RESEARCH ARTICLE

Determination of oxygen relaxivity in oxygen nanobubbles at 3 and 7 Tesla

Emma Bluemke[1] · Liam A. J. Young[2] · Joshua Owen[3] · Sean Smart[4] · Paul Kinchesh[4] · Daniel P. Bulte[1] · Eleanor Stride[1]

Abstract

Objective Oxygen-loaded nanobubbles have shown potential for reducing tumour hypoxia and improving treatment outcomes, however, it remains difficult to noninvasively measure the changes in partial pressure of oxygen (PO_2) in vivo. The linear relationship between PO_2 and longitudinal relaxation rate (R_1) has been used to noninvasively infer PO_2 in vitreous and cerebrospinal fluid, and therefore, this experiment aimed to investigate whether R_1 is a suitable measurement to study oxygen delivery from such oxygen carriers.

Methods T_1 mapping was used to measure R_1 in phantoms containing nanobubbles with varied PO_2 to measure the relaxivity of oxygen (r_{1Ox}) in the phantoms at 7 and 3 T. These measurements were used to estimate the limit of detection (LOD) in two experimental settings: preclinical 7 T and clinical 3 T MRI.

Results The r_{1Ox} in the nanobubble solution was 0.00057 and 0.000235 s^{-1}/mmHg, corresponding to a LOD of 111 and 103 mmHg with 95% confidence at 7 and 3 T, respectively.

Conclusion This suggests that T_1 mapping could provide a noninvasive method of measuring a > 100 mmHg oxygen delivery from therapeutic nanobubbles.

Keywords Quantitative MRI · MRI relaxometry · Oxygen · Hypoxia

Abbreviations

LOD	Limit of detection
MOLLI	Modified look-locker inversion recovery
PO_2	Partial pressure of oxygen
r_{1Ox}	Relaxivity of oxygen
R_1	Longitudinal relaxation rate
ShMOLLI	Shortened modified look-locker inversion recovery
SO_2	Blood oxygen saturation
T_1	Longitudinal relaxation time
VFA	Variable flip angle

✉ Emma Bluemke
emma.bluemke@new.ox.ac.uk

1 Department of Engineering Sciences, Institute of Biomedical Engineering, University of Oxford, Oxford, UK

2 Radcliffe Department of Medicine, Oxford Centre for Clinical Magnetic Resonance Research, University of Oxford, Oxford, UK

3 Clinical Center, National Institutes of Health, Bethesda, MD, USA

4 Department of Oncology, Radiobiology Research Institute, University of Oxford, Oxford, UK

Introduction

Tumour hypoxia is a predictor of disease progression, treatment failures, and metastatic potential in multiple types of cancer [1–4]. Strategies for treating hypoxia have included methods such as blood transfusions, hypoxia-selective drugs, and direct oxygen delivery [5]. The primary methods for oxygen delivery have generally focused on: hyperbaric oxygen or high oxygen content breathing therapy, oxygen-generating materials, and oxygen-carrying materials [6–8]. More recent approaches to hypoxia mitigation have taken advantage of developments in drug-delivery systems to deliver oxygen to the tumour. Of these drug-delivery approaches, therapeutic and diagnostic applications of nano- and micro-materials are playing increasingly important roles [9], such as micro and nanobubbles which can be used to encapsulate oxygen [10–16]. McEwan et al. [13] have shown impressive results using microbubble-delivered oxygen for improving

sonodynamic therapy in pancreatic tumours, Eisenbrey et al. [17] have successfully increased breast tumour oxygenation levels in vitro by 20 mmHg, and Owen et al. [16, 18] have demonstrated that oxygen nanobubbles enhanced tumour response to sonodynamic therapy. These results have illustrated the potential of oxygen loaded nano- and microbubbles to deliver oxygen to the tumour microenvironment, reduce tumour hypoxia, and improve treatment outcomes [13, 16].

However, despite the enhanced therapeutic responses, statistically significant changes in tumour oxygenation were not always observed when this was directly measured [13, 17, 18]. This makes it extremely difficult to establish the underpinning mechanism(s) by which the micro/nanobubbles are promoting therapeutic effects. A key challenge has been that the methods available for measuring changes in oxygenation have multiple limitations. For example, Owen et al. [18] used a single fibre-optic probe and were only able to probe one spot in the tumour. Since tumours are highly heterogeneous in terms of perfusion, this resulted in a very high variability in the measurements. Alternatively, techniques may only be suitable for measuring either dissolved oxygen or oxygen bound to haemoglobin and thus not able to detect oxygen encapsulated within bubbles. For example, Eisenbrey et al. were unable to detect any change in oxygenation using photoacoustic imaging, but this is unsurprising since it relies on comparing ratios of oxygenated and deoxygenated haemoglobin, whereas the delivery of oxygen using micro- and nanobubbles is independent of haemoglobin transport [19]. Therefore, to continue effective research on promising oxygen carriers and hypoxia reduction, robust methods for measuring oxygen delivery from these carriers are needed.

The ideal method should be noninvasive and quantitative, allowing tumour oxygen measurements to be obtained before, during, and after treatment. As magnetic resonance imaging (MRI) is a widely clinically available, non-ionizing, noninvasive imaging technique, it is very well suited for determining tissue oxygenation. Molecular oxygen is paramagnetic [20–27], and it has been demonstrated experimentally repeatedly that the relaxation rate of the imaged material, R_1, is linearly proportional to the concentration or partial pressure of oxygen (PO_2) [21, 28–40]:

$$R_{1Ox} = R_{10} + r_{1Ox} \times C, \tag{1}$$

where R_{1Ox} is the relaxation rate with oxygen added, R_{10} is the relaxation rate without oxygen, C is the concentration or partial pressure of oxygen, and r_{1Ox} is the relaxivity of oxygen in the imaged material (whose units depend on the oxygen measurement used for C). Since the partial pressure of oxygen (PO_2) is a common measurement in biomedicine and clinical applications, in this manuscript, we report C as PO_2 in mmHg and r_{1Ox} as s^{-1}/mmHg.

This linear, reproducible relationship between PO_2 and R_1 has been used to infer oxygen levels in vitreous fluid as a noninvasive alternative to the highly invasive oxygen electrodes used to measure retinal hypoxia [28, 30, 39, 41], bladder urine [41] and urine in the renal pelvis to create a noninvasive detection of renal dysfunction [42], cerebrospinal fluid [33, 41], brain tissue [43, 44], and blood, including foetal blood [36, 45, 46]. Therefore, we hypothesized that this method could also be applicable as a noninvasive method for measuring oxygen delivery from these nanocarriers.

However, changes in R_1 are not specific to oxygen: the R_1 of the material can be affected by the temperature [39, 41], pH [47], protein concentration [30], field strength [48], and numerous other changes in the chemical environment [49]. Therefore, unless the specific PO_2–R_1 relationship was measured in the material of interest previously (with consistent temperature, scanner protocol, and protein concentration), absolute oxygen levels cannot be inferred from R_{10} [41], only a relative change in oxygenation, since the y-intercept of the linear relationship is not known. The nanobubbles used for oxygen delivery in the studies discussed above are small lipid-based particles, ~ 100 nm in diameter, within an acidic (pH 2.3) solution. The relaxivity of oxygen in this nanobubble mixture has not yet been measured, however, analogous work by Thompson et al. demonstrated a measurable change in oxygenation in a phantom before and after destruction of oxygen-filled microbubbles [50]. Thompson et al. found that the linear relationship between PO_2 and R_1 in a phantom containing microbubble solutions of varying PO_2 showed a relaxivity of 0.0003 s^{-1}/mmHg at 7 T. With a similar objective, Vatnehol et al. measured the relaxivity and limit of detection of oxygen at 3 T in "oxygen-enriched" water intended for therapeutic oxygen delivery [37].

We have built upon their work in the experiments in this manuscript to investigate whether MRI T_1 mapping is a suitable technique to examine oxygen delivery from such carriers. Therefore, we hypothesized that this method could also be applicable as a noninvasive method for measuring oxygen delivery from these nanocarriers and that the additional substances in the nanobubble solution would not interrupt the linear relationship between R_1 and PO_2 in the solution. To examine this, we performed two separate experiments to find the relaxivity and limit of detection of oxygen in this nanobubble mixture in two experimental scenarios: a preclinical 7 T MRI and clinical 3 T MRI.

Methods

Phantom design

For the 7 T experiment phantom, seven vials containing different solutions were prepared: oxygen-filled nanobubbles,

nitrogen-filled nanobubbles, air-filled nanobubbles, water, oxygenated water, and a half oxygen-filled and half nitrogen-filled nanobubble mixture. One 0.5 ml syringe was filled per solution and sealed using Cristaseal wax (ProSciTech Pty Ltd, Australia). A seven-chamber custom-built holder was used to hold seven 0.5 ml syringes in the scanner for the duration of the phantom experiment.

For the 3 T experiment phantom, glass vials (10 ml) containing different solutions were prepared: five vials of air-filled nanobubbles, five vials of oxygen-filled nanobubbles, five vials of water, and five vials of water sparged with 100% oxygen. All nanobubble and water solutions were prepared according to the method listed in the section below. The vials were placed in a cylindrical vessel with saline solution surrounding them for the duration of the phantom experiment.

Lastly, to examine the effect that temperature may have on the experiment, three phantom tubes from a calibration phantom (Eurospin II TO5 phantom, Diagnostic Sonar LTD, Livingston, Scotland) were used in the scanner and a Variable Flip Angle (VFA) T_1 map acquired five times, while monitoring the temperature. The three phantom tubes had nominal T_1 values of 830, 1020, and 1350 ms.

Nanobubble preparation

All nanobubble solutions were prepared according to the following method: lecithin and citric acid were obtained from Special Ingredients (Chesterfield, Derbyshire, UK). Glycyrrhizic acid and glycerol were obtained from Sigma-Aldrich Ltd (Gillingham, Dorset, UK). Oxygen and nitrogen cylinders were obtained from BOC gases (Guildford, Surrey, UK). The nanobubble solutions were prepared according to Owen et al. (2016). To create one 100 ml bottle of the solution, glycyrrhizic acid (0.5 mg/ml), lecithin (3 mg/ml), citric acid (5 mg/ml) and glycerol (0.0125 ml/ml) were mixed with 100 ml of freshly boiled, filtered deionized water. The solution was then stirred for 30 min, while it cooled to room temperature. The vial was then immediately sealed and mechanically agitated for 30 s. To produce oxygen-laden nanobubbles, 5 ml of the solution was transferred to a glass vial and sparged with oxygen gas, for 3 min. To produce nitrogen or air-laden nanobubbles, the solution was sparged with nitrogen gas or air for 3 min. The nanobubble size distribution measurements were ascertained using a nanoparticle tracking analyzer (NTA) (Nanosight NS300, Malvern, PA) and all size distributions were consistent with results published by Owen et al. [16].

MRI acquisition details

The 7 T imaging experiments were performed using a 7.0 T 210 mm horizontal bore VNMRS preclinical imaging system equipped with 120 mm bore gradient insert (Varian Inc.

Palo Alto, CA, USA). A variable flip-angle T_1 map [51] was calculated using non-linear least squares from 3D RF and gradient spoiled gradient-echo sequence with 16 flip angles (TR = 3.2 ms, TE = 0.664 ms, matrix = 128×64×64, FA = 1, 1.2, 1.4, 1.6, 1.8, 2, 2.2, 2.4, 2.7, 3.1, 3.7, 4.4, 5.2, 6.1, 7, 8, FOV = 54×27×27 mm^3), and B1 correction was applied using Actual Flip Angle method [52]. The 16 flip angles were chosen according to the Ernst angle for a large range of values of tissue T_1—using more flip angles allows for a more accurate fit for the calculation of T_1. T_1 values were measured and averaged in a region of interest (ROI) placed lengthwise along each syringe to produce a mean T_1 value for each syringe.

The 3 T imaging experiments were performed using a 3.0 T Siemens Prisma MRI (Erlangen, Germany). The VFA T_1 maps were calculated from a linear fit of [51] 3D gradient-echo images with five different flip angles (TR = 4.1 ms, TE = 1.23 ms, FA = 3, 6, 9, 12, 15, slice thickness = 3 mm). The Modified Look-Locker Inversion Recovery (MOLLI) [53] and Shortened Modified Look-Locker Inversion Recovery (ShMOLLI) T_1 maps were calculated from a non-linear fit using a MOLLI T_1-mapping sequence (TR = 3.5 ms, TE = 1.05 ms, 11 inversion times, FA = 35, slice thickness = 8 mm), and Shortened Modified Look-Locker Inversion Recovery (ShMOLLI with the acquisition details: (ShMOLLI_192i protocol, TR = 371.84 ms, TE = 1.01 s, FA = 35, slice thickness = 8 mm, 7 inversion times TI = 100, 1100, 2100, 3100, 4100, 180, 260 ms). Each type of T_1 map was acquired multiple times, repeated in the following order: ShMOLLI 1, MOLLI 1, VFA 1, ShMOLLI 2, MOLLI 2, VFA 2, ShMOLLI 3, MOLLI 3. The ShMOLLI T_1-mapping method produced the lowest standard deviation within each vial ROI and was, therefore, used for the relaxivity and limit of detection (LOD) calculations (see Supplementary Figure S1). Although multiple T_1 maps were acquired for this experiment, the ShMOLLI T_1 map acquired closest to the time point of the collection of the oxygen measurement (ShMOLLI 3) was used to calculate the following relaxivity and LOD results. This decision was made for two reasons: (1) the ShMOLLI 3 and MOLLI 3 data was acquired closest to the time the oxygen measurements were made, and thus provide the T_1 measurement most closely corresponding to the measured PO_2 if oxygen levels were leaking or decreasing over time; and (2) the ShMOLLI T_1 map was chosen over the MOLLI T_1 map due to an artefact corruption on the MOLLI T_1 map. The T_1 measurement from each repetition of the 3 ShMOLLI T_1 maps was compared in Supplementary Figure S2.

The resulting T_1 maps used for analysis are shown in Supplementary Figure S3. Note that the scale bars highlights the size differences between the phantoms, and therefore the field of view shown in each image: the 7 T phantom used small 0.5-ml syringe vials to fit into a small-bore preclinical

scanner, while the 3 T phantom used much larger 10 ml glass vials within a large saline bucket. The resolution of the ShMOLLI image is 1.7 mm × 1.7 mm, and the resolution for the VFA slice displayed was 0.5 mm × 0.5 mm.

Oxygen measurements

Following the 7 T scans, the remaining solution in each of the seven larger vials was measured using a fibre-optic oxygen sensor. All PO_2 measurements were carried out using a PreSens OXY Mini-fibre-optic oxygen meter in combination with SP-PSt3-NAU oxygen sensor spots inside sealed glass vials (PreSens Precision Sensing GmbH, Regensburg, Germany). All oxygen measurements were calibrated and carried out at room temperature according to PreSens manual with oxygen-free water and air-saturated water, as performed by Owen et al. [16, 18].

Following the 3 T scans, the phantom was carefully removed from the scanner, and one by one, each vial was quickly opened and poured into a vial with a PreSens sensor sticker with the PreSens tip recording the PO_2 measurement (PreSens OXY Mini fibre-optic oxygen meter). The PO_2 was recorded for 30 s, recording one measurement per second. All oxygen measurements were calibrated and carried out at room temperature. The oxygenated samples were recorded first, then the non-oxygenated samples, to reduce the time over which the oxygen levels could be decreasing due to exchange with the room air.

Calculation of limit of detection

The limit of detection of oxygen in the solutions can be calculated by the following equation [54]:

$$\mathrm{LOD} = \frac{F \times \mathrm{SD}}{b}, \tag{2}$$

where b is the slope of the regression line (relaxivity, or r_{1Ox}), SD is the standard deviation of the intended in vivo situation, and F is a factor set to 2.2 for LOD calculations with 95% confidence intervals. This method is used by Vatnehol et al. to calculate the limit of detection of dissolved oxygen in water [37].

Results

Oxygen relaxivity

The phantoms and resulting T_1 maps can be seen in Supplementary Figure S3. We measured a strong linear relationship ($R^2 = 0.97$ and $R^2 = 0.97$) between PO_2 and R_1 in the nanobubble solution in vitro at 7 and 3 T, respectively, shown in Fig. 1. The relaxivity (r_{1Ox}) at 7 and 3 T was 0.00024 s^{-1}/mmHg and 0.00057 s^{-1}/mmHg, respectively, and the corresponding upper and lower confidence intervals and P values are listed in Table 1.

Fig. 1 The mean R_1 values (s^{-1}) and mean PO_2 values (mmHg) in the nanobubble solutions at 7 T and 3 T, plotted with a linear regression line ($R^2 = .97$ and $R^2 = .97$) and relaxivity slope (r_{1Ox}) of 0.000235 s^{-1}/mmHg and 0.00057 s^{-1}/mmHg, respectively. The corresponding upper and lower confidence intervals and P values are listed in Table 1. To view this figure with cropped axes, see Supplementary Figure S6
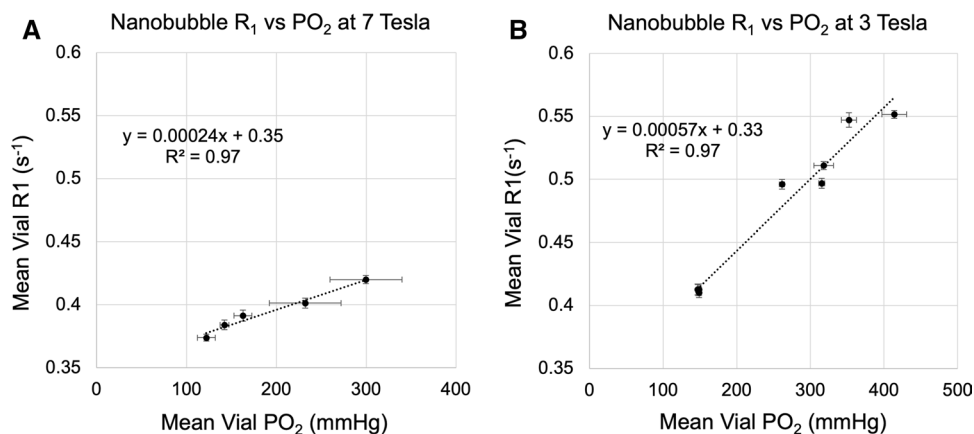
Table 1 The resulting R^2, P value and slope with lower and upper 95% confidence intervals and for each linear regression shown in Fig. 1

Data	Slope (95% CI) [units]	P value	R^2
R_1 vs PO_2 at 7 T (Fig. 2A)	0.00024 (0.00016, 0.00031) [s^{-1}/mmHg]	< 0.0001	0.97
R_1 vs PO_2 at 3 T (Fig. 2B)	0.00057 (0.00048, 0.00065) [s^{-1}/mmHg]	0.00016	0.97

Limit of detection

The SD in the LOD equation represents the standard deviation of the method in the intended tissue. Therefore, for the 7 T preclinical setting, the mean of eight reported standard deviation values of R_1 from the intended experimental tissue—a preclinical tumour model—was calculated, which was approximately 0.011 s^{-1} [55]. Using the measured relaxivity at 7 T (0.000235 s^{-1}/mmHg) and Eq. 1, the resulting LOD (95% confidence) at 7 T in a preclinical tumour model is 103 mmHg. For the 3 T clinical setting, the mean of 11 reported standard deviation values of R_1 from clinical tumour ROI was calculated, which was approximately 0.029 s^{-1} [56]. Using the measured relaxivity at 3 T (0.00057 s^{-1}/mmHg) and Eq. 1, the resulting LOD (95% confidence) at 3 T in a clinical tumour is 111 mmHg. Of course, it is likely that measurements from T_1 mapping methods will be less precise in vivo than in phantoms—therefore, in vivo measurements for SD were used in these LOD calculations.

Nanobubbles and R_1

In comparison to water, the nanobubble solution contains several attributes that may affect R_1, in particular, the presence of the lipid-based particles, and the acidity (pH 2.3) of the solution. It was apparent from both the 7 and 3 T experiments (Fig. 2) that the nanobubble solution alone—*without* oxygen added—produced an increase in R_1 of 0.03 and 0.07 s^{-1} compared to water; equivalent to increasing the water PO_2 by 230 and 130 mmHg (at 7 and 3 T, respectively).

The experiment measuring the effect of temperature on R_1 showed that the R_1 of all three tubes decreased as temperature increased, and a linear regression fit strongly ($R^2 = 0.83$, 0.90, 0.91). The change in R_1 per change in temperature was -0.037, -0.027, and -0.020 s^{-1}/°C for the three tubes, respectively (see Supplementary Figure S4), and a steeper slope corresponded to a higher baseline R_1, and vice versa. The corresponding upper and lower confidence intervals

and P values are listed in Supplementary Table S1. This means that from just a 0.5 °C fluctuation in temperature, in R_1 would change by 0.018 s^{-1}, which would correspond to a 32 and 77 mmHg inaccuracy in PO_2 estimation, at 3 and 7 T, respectively. The same data are also provided in terms of T_1 in Supplementary Figure S5, where a linear regression fit T_1 vs temperature data strongly as well ($R^2 = 0.83$, 0.90, 0.91) with a slope of 20, 23, and 29 ms/°C for the three tubes, respectively. These results are consistent with findings by Zhang et al. where the temperature sensitivity increased with baseline T_1, following closely a second-order polynomial (see Fig. 2 in Zhang et al.) [57].

Discussion

The relationship between PO_2 and R_1 has been used to noninvasively infer oxygen levels in vitreous fluid [28, 30, 39, 41], urine [41, 42], cerebrospinal fluid [33, 41], brain tissue [43, 44], and blood [36, 45, 46]. Therefore, we hypothesized that this method could also be applicable as a noninvasive method for measuring oxygen delivery from these nanocarriers. To examine this, we performed two separate experiments to find the relaxivity and limit of detection of oxygen in this nanobubble mixture in two experimental scenarios: a preclinical 7 T MRI and clinical 3 T MRI.

Relaxivity

These experiments reproduced the linear R_1–PO_2 relationship expected ($R^2 = 0.97$), and showed that the PO_2 of the nanobubble solution could be estimated using T_1 mapping at 7 and 3 T. It was a possibility that the composition of the nanobubble solution would interrupt this linear R_1–PO_2 relationship or induce image artefacts. Fortunately, this was not found to be the case.

The r_{1Ox} in the nanobubble solution was 0.00024 and 0.00057 s^{-1}/mmHg at 7 and 3 T respectively. In these experiments, the r_{1Ox} was stronger at the lower field strength, which agrees with other reports from phantom

Fig. 2 The mean R_1 and PO_2 values of the vials of water and oxygenated water (black crosses), in comparison to non-oxygenated nanobubbles (red cross), at **A** 7 T and **B** 3 T. The contents of the non-oxygenated nanobubble solution resulted in an R_1 that was 0.03 and 0.07 s^{-1} higher than water, the equivalent effect as increasing the water PO_2 by 230 and 130 mmHg (at 7 and 3 T, respectively)
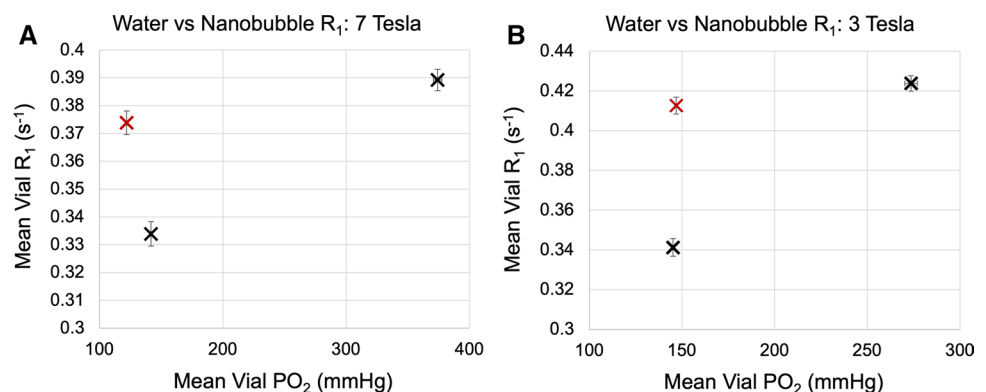
measurements of r_{1Ox} being greater at lower field strengths [58–60]. The comparable experiments by Thompson et al. [50] found an r_{1Ox} of 0.0003 s^{-1}/mmHg at 7 T, which within the upper 95% confidence interval of our measurement performed at 7 T (0.00031 s^{-1}/mmHg). Therefore, even though the composition of the microbubble solution and nanobubble solutions differ considerably (see Thompson et al. [50] for the microbubble formula), the r_{1Ox} seems to be almost independent of the nano or microbubble composition, which is a notable strength of this method.

Limit of detection

Using our measured r_{1Ox} and published values of the expected standard deviation in R_1 within preclinical and clinical tumour tissue, the resulting 95% confidence interval LOD calculated indicates that a 103 mmHg (4.56 mg/L) and 111 mmHg (or 7.04 mg/L) increase in oxygen is required to reliably detect a change in R_1 from oxygen delivery (in a preclinical and clinical setting, respectively). These are both slightly lower than the 8.5–12.3 mg/L limit of detection estimated by Vatnehol et al., however, for their calculations, the authors use the standard deviation in the hepatic portal vein as that is their material of interest [37]. Of course, this raises the most important point of this discussion: these LOD calculations assume that there are no other potential T_1 changing effects present other than an increase in oxygen—which, in the body, is an often unrealistic assumption, especially in a voxel containing blood. The other main endogenous paramagnetic material in the body is deoxyhemoglobin, and the R_1 of blood decreases linearly as oxygen saturation increases (i.e. as deoxyhemoglobin is converted to oxyhemoglobin, which is diamagnetic) [34, 61, 62]. Only following full oxygen saturation ($SO_2 > 99\%$) will the R_1 of blood increase linearly due to the increase in the PO_2 of the plasma being the dominant remaining effect [29, 34, 36, 45, 62]. Therefore, if an oxygen delivery method results in an increase in oxygen saturation of the blood, it is likely to induce a *negative* change in R_1 first, until it delivers enough oxygen to reach full saturation [62]. In fact, this is precisely what was observed by Vatnehol et al. when they performed their intended oxygen delivery experiment in humans and measured a *negative* R_1 change in the blood [63]. However, for a voxel that does not contain 100% blood, such as normal tissue, it has been demonstrated that the R_1 of the tissue will increase linearly with the level of dissolved oxygen in the tissue [43]. Since the effect from changing deoxyhemoglobin levels will only pertain to the percent volume in the voxel that is occupied by blood, then the remaining 90–98% of voxel volume will be dominated by R_1 change of the tissue. In addition to deoxyhemoglobin, iron levels present in the tissue would affect R_1 as well, and it can accumulate depending on the disease and organ. Therefore, while the

LOD calculations in this manuscript do not account for confounding effects on R_1, they are still useful to obtain an estimation of whether the detection of nanobubble oxygen delivery by R_1 measurement is feasible.

The expected PO_2 change in the tumour tissue following the administration of nanobubbles has been reported to be approximately 30 mmHg, albeit this was measured using a method that was likely underestimating the PO_2 [16]. This is much lower than both the LODs calculated in this experiment (103 and 111 mmHg), however this LOD calculation is stating that the two peaks of the distributions are separated by 2.2 standard deviations, which is considerable. Therefore, although the expected oxygen delivery is below the measured LOD, this could still be a feasible method for detecting the expected change in PO_2. In addition, this measurement describes the LOD for a single voxel, which is different from the detection power in a large ROI—due to the repeated number of voxel measures in a large ROI, it would be feasible to detect a much smaller difference between two large ROIs that would otherwise not be realistic in a single voxel. Furthermore, the limit of detection will depend not only on the tumour type, and in particular its T_1 values at a particular magnetic field, but also the site of the tumour—such as the head and neck region versus the pelvic region—which will affect the SNR characteristics, and may be a caveat to this estimate.

In addition, the standard deviation within the tumour ROIs used is a combination of both tissue heterogeneity and T_1 mapping measurement variability, and as T_1 mapping methods continue to improve, it is possible that the standard deviations could decrease significantly and oxygen detection could be made on a voxel-wise level. Therefore, although the resulting LODs calculated from this experiment are greater than the expected PO_2 change, it is possible that as T_1 mapping techniques become more stable, assessment of spatial variation of PO_2 may then be possible compared to region averaging which is needed currently, enabling T_1 mapping to be a suitable technique to examine oxygen delivery from these nanobubbles.

Lastly, the LOD measurement describes the sensitivity of this technique to detecting PO_2 changes in an individual. As a paired measurement in a study across multiple subjects at 3 T, however, assuming that a similar standard deviation as previous clinical R_1 measurements [56], then a study of 10, 13, or 15 participants would yield 80%, 90%, or 95% power, respectively (alpha 0.05) [64].

Additional confounding effects

In comparison to water, the increased lipid content and acidity of the non-oxygenated nanobubble solution resulted in an R_1 that was higher than water. The magnitude of this effect was the equivalent of increasing the water PO_2 by 230 and 130 mmHg (at 7 and 3 T, respectively). Thus, it is likely that increasing the nanobubble concentration in a water or saline

phantom solution would increase R_1, making it difficult to use that change in signal to infer a change in PO_2. This problem is similar to that reported by Vatnehol et al. [63], where the delivery of a dissolved oxygen water drink caused a dilution that changed R_1 in both the control drink and the oxygen drink. It is possible that this dilution would be a negligible effect from the nanobubbles once spread out in the circulatory system, however, it could make oxygen nanobubble delivery indistinguishable from non-oxygenated nanobubble delivery. Since the percent volume of nanobubble solution would be far below 10% of the blood volume and the tissue voxel would contain below 10% blood volume, and since the low pH would be neutralized in the bloodstream, it is reasonable to conclude that this confound would not be as substantial as the R_1 change from the PO_2 change within the tissue dominating 85–98% of the voxel volume, assuming a range of fractional blood volume in tumours of approximately 2–15% [65].

There are additional remaining factors that can affect R_1. Experiments using R_1 to measure PO_2 in vitreous fluid have demonstrated the strong effect of temperature on the R_1 measurement [39, 41]. Unfortunately, this is not insignificant—Zaharchuk et al. reported that based on their phantom experiments, they found a potential error ± 19 mmHg for physiologic temperature fluctuations of ± 1 °C [41]. We believe this drift in R_1 values shown in Supplementary Figure S2 is due to a combination of two factors: (1) the temperature of the vials increasing due to absorption of heat from RF field exposure, and (2) a slight decrease in PO_2 in the vials as oxygen may be able to slowly leak out of the vial during the duration of the scanning session. Both of these effects independently would cause a decrease in R_1. This possible decrease in oxygen throughout the scanning session is why ShMOLLI 3, the ShMOLLI acquired closest to the time of oxygen measurement, was used for the analysis.

Experiment limitations

The gold-standard T_1 mapping method to use would have been inversion recovery, since Look-Locker techniques such as ShMOLLI are known to underestimate the true T_1 and VFA will overestimate the true T_1 (seen in Supplementary Figure S1) [66]. However, these experiments were intended as preliminary work for preclinical and clinical experiments, and therefore, it was more appropriate to use the actual experimental set up and scanning techniques that could be used in mice and human volunteers and/or patients. In comparison to phantoms, scanning live subjects introduces issues such as motion from breathing and limitations to scan time, and therefore the faster VFA method and much faster ShMOLLI method were more appropriate than inversion recovery. Lastly, although the T_1 might be over- or underestimated, the *relative* change in R_1 (and therefore r_{1Ox}) should remain the same in each method.

In addition, the 95% confidence interval of the fit of the slope of the measurements was $\pm 30\%$ at 7 T, and $\pm 16\%$ at 3 T, which at first glance, suggests that the T_1 measurements from the 7 T scans were less reliable. However, upon further examination of the underlying data, we believe this discrepancy is due to the oxygen measurements rather than the T_1 measurements. For the two data points with the highest PO_2 in the 7 T data, the PO_2 measurements have larger error bars—this is due to those glass vials showing a larger range of PO_2 during the PreSens measurement time due to being disturbed while being moved from the scanner. Therefore, it is possible that the true PO_2 during the time of T_1 measurement was slightly different than it is showing there, which would result in a slightly tighter alignment of the data points and more narrow CI range. However, the T_1 measurements from the 7 T data were of relatively lower quality than T_1 measurements from the 3 T data, which remains a limitation of this study.

A final noteworthy observation is that adjusting the concentration of nanobubble solution in each vial would also alter the R_1, as shown by the difference between the 'water' vial and 'nanobubble' vial in Fig. 2. We did not perform measurements at multiple concentrations of nanobubbles, so we are unable to provide additional data on this, but we hypothesise that R_1 would decrease change linearly with increasing nanobubble concentration. To clarify, in this experiment, any solution containing nanobubble solution contained the same concentration of nanobubble solution, and the oxygen levels were altered via the gas used, not by the nanobubble concentration.

Conclusion

We measured a strong linear relationship ($R^2 = 0.97$) between PO_2 and R_1 in the nanobubble solution, and measured the relaxivity of oxygen in the nanobubble solution to be 0.00057 s^{-1}/mmHg and 0.000235 s^{-1}/mmHg, and established that a 111 and 103 mmHg increase in oxygen is required to detect a change in R_1 with 95% confidence at 7 and 3 T, respectively. This suggests that T_1 mapping could provide a noninvasive method of measuring a > 100 mmHg oxygen delivery from oxygenated nanobubbles in therapy.

Declarations

Conflict of interest All authors declare that they have no conflict of interest.

Ethical statement The authors of this manuscript certify that they have no affiliations with or involvement in any organization or entity with any financial interest (such as honoraria; educational grants; participation in speakers' bureaus; membership, employment, consultancies, stock ownership, or other equity interest; and expert testimony or patent-licensing arrangements), or non-financial interest (such as personal or professional relationships, affiliations, knowledge or beliefs) in the subject matter discussed in this manuscript. No subjects, animals, or cell lines were used in the experiments in this manuscript.

References

1. Chaudary N, Hill RP (2007) Hypoxia and metastasis. Clin Cancer Res 13:1947–1949
2. Milosevic M, Warde P, Ménard C, Chung P, Toi A, Ishkanian A, McLean M, Pintilie M, Sykes J, Gospodarowicz M, Catton C, Hill RP, Bristow R (2012) Tumor hypoxia predicts biochemical failure following radiotherapy for clinically localized prostate cancer. Clin Cancer Res 18:2108–2114
3. Stewart GD, Ross JA, McLaren DB, Parker CC, Habib FK, Riddick ACP (2010) The relevance of a hypoxic tumour microenvironment in prostate cancer. BJU Int 105:8–13
4. Yuen A, Díaz B (2014) The impact of hypoxia in pancreatic cancer invasion and metastasis. Hypoxia (Auckl) 2:91–106
5. Brown JM (2000) Exploiting the hypoxic cancer cell: mechanisms and therapeutic strategies. Mol Med Today 6:157–162
6. Rockwell S (1989) Tumor radiation responses and tumor oxygenation in aging mice. Exp Gerontol 24:37–48
7. Ogawa Y, Kubota K, Ue H, Tadokoro M, Matsui R, Yamanishi T, Hamada N, Kariya S, Nishioka A, Nakajima H, Tarutani M, Sano S (2011) Safety and effectiveness of a new enzyme-targeting radiosensitization treatment (KORTUC II) for intratumoral injection for low-LET radioresistant tumors. Int J Oncol 39:553–560
8. Tibbles PM, Edelsberg JS (1996) Hyperbaric-oxygen therapy. N Engl J Med 334:1642–1648
9. Anselmo AC, Mitragotri S (2014) An overview of clinical and commercial impact of drug delivery systems. J Control Release Off J Control Release Soc 190:15–28
10. Kheir JN, Scharp LA, Borden MA, Swanson EJ, Loxley A, Reese JH, Black KJ, Velazquez LA, Thomson LM, Walsh BK, Mullen KE, Graham DA, Lawlor MW, Brugnara C, Bell DC, McGowan FX (2012) Oxygen gas-filled microparticles provide intravenous oxygen delivery. Sci Transl Med 4:140ra88
11. Feshitan JA, Legband ND, Borden MA, Terry BS (2014) Systemic oxygen delivery by peritoneal perfusion of oxygen microbubbles. Biomaterials 35:2600–2606
12. Gerber F, Waton G, Krafft MP, Vandamme TF (2009) Long lived microbubbles for oxygen delivery. Artif Cells Blood Substit Biotechnol 35:119–124
13. McEwan C, Owen J, Stride E, Fowley C, Nesbitt H, Cochrane D, Coussios CC, Borden M, Nomikou N, McHale AP, Callan JF (2015) Oxygen carrying microbubbles for enhanced sonodynamic therapy of hypoxic tumours. J Control Release 203:51–56
14. Yang C, Xiao H, Sun Y, Zhu L, Gao Y, Kwok S, Wang Z, Tang Y (2018) Lipid microbubbles as ultrasound-stimulated oxygen carriers for controllable oxygen release for tumor reoxygenation. Ultrasound Med Biol 44:416–425
15. Zhu W, Dong Z, Fu T, Liu J, Chen Q, Li Y, Zhu R, Xu L, Liu Z (2016) Modulation of hypoxia in solid tumor microenvironment with MnO_2 nanoparticles to enhance photodynamic therapy. Adv Funct Mater 26:5490–5498
16. Owen J, Logan K, Nesbitt H, Able S, Vasilyeva A, Bluemke E, Kersemans V, Smart S, Vallis KA, McHale AP, Callan JF, Stride E (2021) Orally administered oxygen nanobubbles enhance tumor response to sonodynamic therapy. Nano Select. https://doi.org/10.1002/nano.202100038
17. Eisenbrey JR, Shraim R, Liu J-B, Li J, Stanczak M, Oeffinger B, Leeper DB, Keith SW, Jablonowski LJ, Forsberg F, O'Kane P, Wheatley MA (2018) Sensitization of hypoxic tumors to radiation therapy using ultrasound sensitive oxygen microbubbles. Int J Radiat Oncol Biol Phys. https://doi.org/10.1016/j.ijrobp.2018.01.042
18. Owen J, McEwan C, Nesbitt H, Bovornchutichai P, Averre R, Borden M, McHale AP, Callan JF, Stride E (2016) Reducing tumour hypoxia via oral administration of oxygen nanobubbles. PLoS ONE 11:e0168088
19. Needles A, Heinmiller A, Sun J, Thcodoropoulos C, Bates D, Hirson D, Yin M, Foster SF (2013) Development and initial application of a fully integrated photoacoustic micro-ultra-sound system. IEEE Trans Ultrason Ferroelectr Freq Control 60:888–897
20. Bloembergen N (1957) Proton relaxation times in paramagnetic solutions. J Chem Phys 27:572–573
21. Chiarotti G, Cristiani G, Giulotto L (1955) Proton relaxation in pure liquids and in liquids containing paramagnetic gases in solution. Il Nuovo Cimento 1955–1965(1):863–873
22. Mel'nichenko NA, (2008) The solubility of oxygen in sea water and solutions of electrolytes according to the pulse proton NMR data. Russ J Phys Chem A 82:1533–1539
23. Mirhej ME (1965) Proton spin relaxation by paramagnetic molecular oxygen. Can J Chem 43:1130–1138
24. Parker DS, Harmon JF (1974) Dipolar spin-lattice relaxation in water containing oxygen. Chem Phys Lett 25:505–506
25. Solomon I (1955) Relaxation processes in a system of two spins. Phys Rev 99:559–565
26. Torrey HC (1953) Nuclear spin relaxation by translational diffusion. Phys Rev 92:962–969
27. Young IR, Clarke GJ, Baffles DR, Pennock JM, Doyle FH, Bydder GM (1981) Enhancement of relaxation rate with paramagnetic contrast agents in NMR imaging. J Comput Tomogr 5:543–547
28. Berkowitz BA, Wilson CA (1995) Quantitative mapping of ocular oxygenation using magnetic resonance imaging. Magn Reson Med 33:579–581
29. Berkowitz BA (1997) Role of dissolved plasma oxygen in hyperoxia-induced contrast. Magn Reson Imaging 15:123–126
30. Simpson ARH, Dowell NG, Jackson TL, Tofts PS, Hughes EH (2013) Measuring the effect of pars plana vitrectomy on vitreous

oxygenation using magnetic resonance imaging effects of PPV on pO_2 using MRI. Investig Ophthalmol Vis Sci 54:2028–2034

31. Nestle N, Baumann T, Niessner R (2003) Oxygen determination in oxygen-supersaturated drinking waters by NMR relaxometry. Water Res 37:3361–3366

32. Matsumoto K, Bernardo M, Subramanian S, Choyke P, Mitchell JB, Krishna MC, Lizak MJ (2006) MR assessment of changes of tumor in response to hyperbaric oxygen treatment. Magn Reson Med 56:240–246

33. Zaharchuk G, Martin AJ, Rosenthal G, Manley GT, Dillon WP (2005) Measurement of cerebrospinal fluid oxygen partial pressure in humans using MRI. Magn Reson Med 54:113–121

34. d'Othée BJ, Rachmuth G, Munasinghe J, Lang EV (2003) The effect of hyperoxygenation on T1 relaxation time in vitro1. Acad Radiol 10:854–860

35. Kramer H, Corcos A, Hernando D, Berry J, Schiebler M, Reeder S (2013) Effekt von molekularem Sauerstoff auf Relaxationszeiten bei klinischen Feldstärken. Fortschr Röntgenstr. https://doi.org/10.1055/s-0033-1346217

36. Pilkinton DT, Hiraki T, Detre JA, Greenberg JH, Reddy R (2012) Absolute cerebral blood flow quantification with pulsed arterial spin labeling during hyperoxia corrected with the simultaneous measurement of the longitudinal relaxation time of arterial blood. Magn Reson Med 67:1556–1565

37. Vatnehol SAS, Hol PK, Bjørnerud A, Amiry-Moghaddam M, Haglerød C, Storås TH (2020) Determination of oxygen r1 at 3 tesla using samples with a concentration range of dissolved oxygen. Magn Reson Mater Phy 33:447–453

38. Hausser R, Noack F (1965) Kernmagnetische Relaxation und Korrelation im System Wasser - Sauerstoff. Zeitschrift für Naturforschung A 20:1668–1675

39. Muir ER, Zhang Y, Nateras OSE, Peng Q, Duong TQ (2013) Human vitreous: MR imaging of oxygen partial pressure. Radiology 266:905–911

40. Hueckel P, Schreiber W, Markstaller K, Bellemann M, Kauczor H-U, Thelen M (2000) Effect of partial oxygen pressure and hematocrit on T1 relaxation in human blood. In: Proceedings of the international society for magnetic resonance in medicine 1586.

41. Zaharchuk G, Busse RF, Rosenthal G, Manley GT, Glenn OA, Dillon WP (2006) Noninvasive oxygen partial pressure measurement of human body fluids in vivo using magnetic resonance imaging. Acad Radiol 13:1016–1024

42. Wang ZJ, Joe BN, Coakley FV, Zaharchuk G, Busse R, Yeh BM (2008) Urinary oxygen tension measurement in humans using magnetic resonance imaging. Acad Radiol 15:1467–1473

43. Beeman SC, Shui Y-BB, Perez-Torres CJ, Engelbach JA, Ackerman JJ, Garbow JR (2016) O₂-sensitive MRI distinguishes brain tumor versus radiation necrosis in murine models. Magn Reson Med 75:2442–2447

44. Haddock B, Larsson HBW, Hansen AE, Rostrup E (2013) Measurement of brain oxygenation changes using dynamic T1-weighted imaging. Neuroimage 78:7–15

45. Silvennoinen MJ, Kettunen MI, Kauppinen RA (2003) Effects of hematocrit and oxygen saturation level on blood spin-lattice relaxation. Magn Reson Med 49:568–571

46. Portnoy S, Seed M, Sled JG, Macgowan CK (2017) Non-invasive evaluation of blood oxygen saturation and hematocrit from T1 and T2 relaxation times: in-vitro validation in fetal blood. Magn Reson Med 78:2352–2359

47. Moser E, Winklmayr E, Holzmüller P, Krssak M (1995) Temperature- and pH-dependence of proton relaxation rates in rat liver tissue. Magn Reson Imaging 13:429–440

48. Rooney WD, Johnson G, Li X, Cohen ER, Kim S-G, Ugurbil K, Springer CS (2007) Magnetic field and tissue dependencies of human brain longitudinal ^1H_2O relaxation in vivo. Magn Reson Med 57:308–318

49. Kaldoudi E, Williams SCR (1993) Relaxation time measurements in NMR imaging. Part I: longitudinal relaxation time. Concepts Magn Reson 5:217–242

50. Thompson E, Smart S, Kinchesh P, Bulte D, Stride E (2019) Magnetic resonance imaging of oxygen microbubbles. Healthc Technol Lett 6:138–142

51. Cheng H, An W-G, in, (2006) Rapid high-resolution T1 mapping by variable flip angles: accurate and precise measurements in the presence of radiofrequency field inhomogeneity. Magn Reson Med. https://doi.org/10.1002/mrm.20791

52. Yarnykh VL (2006) Actual flip-angle imaging in the pulsed steady state: A method for rapid three-dimensional mapping of the transmitted radiofrequency field. Magn Reson Med 57:192–200

53. Messroghli DR, Radjenovic A, Kozerke S, Higgins DM, Sivananthan MU, Ridgway JP (2004) Modified look-locker inversion recovery (MOLLI) for high-resolution T1 mapping of the heart. Magn Reson Med 52:141–146

54. Shrivastava A (2011) Methods for the determination of limit of detection and limit of quantitation of the analytical methods. Chron Young Sci 2:21–25

55. Yang DM, Arai TJ, Campbell JW, Gerberich JL, Zhou H, Mason RP (2019) Oxygen-sensitive MRI assessment of tumor response to hypoxic gas breathing challenge. NMR Biomed 32:e4101

56. O'Connor JP, Naish JH, Parker GJ, Waterton JC, Watson Y, Jayson GC, Buonaccorsi GA, Cheung S, Buckley DL, McGrath DM, West CM, Davidson SE, Roberts C, Mills SJ, Mitchell CL, Hope L, Ton NC, Jackson A (2009) Preliminary study of oxygen-enhanced longitudinal relaxation in MRI: a potential novel biomarker of oxygenation changes in solid tumors. Int J Radiat Oncol Biol Phys 75:1209–1215

57. Zhang Q, Werys K, Popescu IA, Biasiolli L, Ntusi NAB, Desai M, Zimmerman SL, Shah DJ, Autry K, Kim B, Kim HW, Jenista ER, Huber S, White JA, McCann GP, Mohiddin SA, Boubertakh R, Chiribiri A, Newby D, Prasad S, Radjenovic A, Dawson D, Schulz-Menger J, Mahrholdt H, Carbone I, Rimoldi O, Colagrande S, Calistri L, Michels M, Hofman MBM, Anderson L, Broberg C, Andrew F, Sanz J, Bucciarelli-Ducci C, Chow K, Higgins D, Broadbent DA, Semple S, Hafyane T, Wormleighton J, Salerno M, He T, Plein S, Kwong RY, Jerosch-Herold M, Kramer CM, Neubauer S, Ferreira VM, Piechnik SK (2021) Quality assurance of quantitative cardiac T1-mapping in multicenter clinical trials—a T1 phantom program from the hypertrophic cardiomyopathy registry (HCMR) study. Int J Cardiol 330:251–258

58. Teng CL, Hong H, Kiihne S, Bryant RG (2001) Molecular oxygen spin-lattice relaxation in solutions measured by proton magnetic relaxation dispersion. J Magn Reson 148:31–34

59. Campbell-Washburn AE, Ramasawmy R, Restivo MC, Bhattacharya I, Basar B, Herzka DA, Hansen MS, Rogers T, Bandettini WP, McGuirt DR, Mancini C, Grodzki D, Schneider R, Majeed W, Bhat H, Xue H, Moss J, Malayeri AA, Jones EC, Koretsky AP, Kellman P, Chen MY, Lederman RJ, Balaban RS (2019) Opportunities in interventional and diagnostic imaging by using high-performance low-field-strength MRI. Radiology 293:384–393

60. Bluemke E, Stride E, Bulte D (2021) A simplified empirical model to estimate oxygen relaxivity at different magnetic fields. NMR Biomed. https://doi.org/10.1002/nbm.4625

61. Blockley NP, Jiang L, Gardener AG, Ludman CN, Francis ST, Gowland PA (2008) Field strength dependence of R 1 and R2* relaxivities of human whole blood to prohance, vasovist, and deoxyhemoglobin. Magn Reson Med 60:1313–1320

62. Bluemke E, Stride E, Bulte D (2021) A general model to calculate the spin-lattice relaxation rate (R1) of blood, accounting for haematocrit, oxygen saturation, oxygen partial pressure, and magnetic field strength under hyperoxic conditions. J Magn Reson Imaging. https://doi.org/10.1002/jmri.27938

63. Vatnehol SAS, Hol PK, Bjørnerud A, Amiry-Moghaddam M, Haglerød C, Storås TH (2020) Effect of drinking oxygenated water assessed by in vivo MRI relaxometry. J Magn Reson Imaging 52:720–728

64. Singh ND (2021) Sample size calculator for comparing paired differences. https://statulator.com/SampleSize/ss2PM.html#. Accessed 4 Oct 2021

65. Qi X-L, Burns P, Hong J, Stainsby J, Wright G (2008) Characterizing blood volume fraction (BVF) in a VX2 tumor. Magn Reson Imaging 26:206–214

66. Stikov N, Boudreau M (2015) On the accuracy of T1 mapping: searching for common ground. Magn Reson Med 73:514–522